Highly Porous Composite Aerogel Based Triboelectric Nanogenerators for High Performance Energy Generation and Versatile Self-Powered Sensing

Journal:	*Nanoscale*
Manuscript ID	NR-ART-07-2018-005872.R1
Article Type:	Paper
Date Submitted by the Author:	31-Oct-2018
Complete List of Authors:	Mi, Hao-Yang; Hunan University of Technology, School of Packaging and Materials Engineering Jing, Xin; University of Wisconsin Madison, Wisconsin Institute for Discovery; South China University of Technology, Department of Industrial Equipment and Control Engineering Cai, Zhiyong; Forest Product Laboratory, Liu, Yuejun; Hunan University of Technology, Key Laboratory of New Materials and Technology for Packaging; Xiamen University of Technology, Key Laboratory of Polymer Processing Principle and Application Turng, Lih-Sheng; University of Wisconsin Madison, Wisconsin Institute for Discovery; University of Wisconsin Madison, Mechanical Engineering Gong, Shaoqin; University of Wisconsin Madison, Materials Science and Engineering; University of Wisconsin Madison, Biomedical Engineering

Highly Porous Composite Aerogel Based Triboelectric Nanogenerators for High Performance Energy Generation and Versatile Self-Powered Sensing

Hao-Yang Mi[a,b,d], Xin Jing[a,b,d], Zhiyong Cai[e], Yuejun Liu[a], Lih-Sheng Turng[b,d], and Shaoqin Gong[b,c*]*

[a] School of Packaging and Materials Engineering, Hunan University of Technology, Zhuzhou, 412007, China
[b] Wisconsin Institutes for Discovery, University of Wisconsin–Madison, Madison, WI 53715, USA
[c] Department of Biomedical Engineering, University of Wisconsin–Madison, Madison, WI 53706, USA
[d] Department of Mechanical Engineering, University of Wisconsin–Madison, Madison, WI 53706, USA
[e] Forest Product Laboratory, USDA, Madison, WI 53726, USA

Footnotes:
Corresponding Authors:
L.S. Turng: turng@engr.wisc.edu; and S. Gong: shaoqingong@wisc.edu

The first and second authors contribute equally to this work.

Abstract

Boosting power generation performance while employing economical and biocompatible materials are ongoing directions in the field of triboelectric nanogenerators (TENGs). Here, highly porous, biocompatible, cellulose nanofibril (CNF) composite-based TENGs are developed through an environmental friendly freeze-drying approach. High tribopositivity materials, including silica fiber, human hair, and rabbit fur, are used as fillers in composite TENG fabrication for the first time to enhance the triboelectric output performance. Among them, a CNF/rabbit fur composite aerogel-based TENG offers the optimum energy generation ability with a high power density of 3.4 W/m^2 achieved on a 4.7 MΩ load under a pressure of 30 kPa. Owing to the high output, the porous composite TENG exhibits an excellent energy harvesting performance and high sensitivity in detecting ultralight forces and monitoring human motion when used as a self-powered sensor. This work introduces a new class of highly porous composite TENGs that integrate biocompatibility, low cost, flexibility, high energy generation performance, and sensing sensitivity, as well as providing new strategies for high performance TENG design and fabrication.

Keywords: triboelectric nanogenerators, cellulose nanofibrils, rabbit fur, highly porous composites, self-powered sensors

Introduction

Harvesting ubiquitous mechanical energy from the ambient environment has emerged with broad interest and pervasive impact due to the rising need for clean and alternative energy resources.[1-3] Triboelectric nanogenerators (TENGs) are capable of harnessing mechanical energy from chaotic motion through the coupling effect of contact electrification and electrostatic induction between two materials that have dissimilar tribopolarities.[4-6]. The dissimilar materials are periodically in contact or separated through different modes of TENG, including contact-separation mode, contact-sliding mode, single-electrode mode, and free-standing triboelectric-layer mode.[7-10] Attributed to the diverse design of TENGs, they have shown the ability to harvest mechanical energy from human motion, machine vibration, wheel rotation, wind, and ocean waves.[11-15] TENGs also possess a special advantage in sensing applications as they do not require an energy supply, which is highly desirable in wearable and implantable devices.[16-18] The current challenges for TENGs include boosting their power generation performance, enhancing sensing sensitivity, reducing fabrication cost, and exploring broad practical applications. Moreover, most fabricated TENGs are made of synthetic polymers and metals that are not renewable, biodegradable, or biocompatible. It is highly preferred to develop novel TENGs based on biocompatible, renewable, and natural resources, which enables their potential biomedical applications and reduces their cost.

Cellulose is the most abundant resource on earth.[19] Cellulose nanofibrils (CNFs) extracted from plants have high aspect ratios, excellent mechanical properties, flexibility, and biocompatibility.[20, 21] Efforts have been made to utilize CNF in TENG applications.[22-24] However, those TENGs suffer from low triboelectric output due to the low tribopositivity of CNF. Thus, CNF normally needs to be chemically modified in TENG applications. According to the triboelectric series, rabbit fur (RF), human hair (HH), and glass are among most tribopositive materials,[25, 26] although they are barely used in TENG fabrication because of the

difficulties in processing RF and HH, and the brittleness of glass. However, it is expected that the tribopositivity of resulting CNF/high tribopositive material composites can be enhanced by simply blending these materials as fillers.

One commonly used approach for enhancing the output performance of TENGs is to introduce micro- and nanoscale topographies on the triboelectric material surface to increase the electrification area.[27-30] However, the process usually involves high cost techniques such as anodic oxidation, laser-assisted machining, etching, and micro-printing.[31-34] Highly porous aerogels that have low cost, lightweight, high surface area, and flexibility have received increased attention for various applications in recent years.[35-38] Furthermore, the porous structure of aerogels not only creates a rough surface, but also provides an immense interior surface area, which might be beneficial for generating additional charges.[23, 35] In addition, the output of TENGs can be enhanced by optimizing the TENG design, such as by integrating it with other energy harvesting devices to result in a hybrid energy cell.[39-41]

Here, we combine the advantages of highly porous aerogels and composite materials and present a new class of low cost, biocompatible, flexible, high performance porous composite TENGs (PCTENG) based on CNF/silica fiber (SF), CNF/HH, and CNF/RF composite aerogels. The CNF/RF composite aerogel based TENG exhibited the best triboelectric output performance with an output voltage and current of 110.0 V and 11.3 μA, respectively. It exhibited a high power density of 3.4 W/m^2 on a 4.7 MΩ load under a low compression pressure of 30 kPa. This unique PCTENG not only can harvest energy and power samll electronics, but also offer high sensitivity in sensing mechaincal motion, light forces, or vibration.

Results and Discussion

The morphologies of these three fibrous fillers are shown in Figure 1A–C. Three-dimensional SFs were fabricated by self-assembly electrospinning of a tetraethyl orthosilicate (TEOS)/polyvinyl alcohol (PVA) solution followed by calcination according to our previous works.[42-44] Figure S1 illustrates the process and a sample of self-assembly electrospun TEOS/PVA 3D fibers. The prepared SFs have a 3D continues fibrous structure with an average fiber diameter of 1.3 ± 0.3 μm, as shown in Figure 1A. These fibers can be easily dispersed in various polymer solutions to prepare composite materials.[45] HHs and RFs are basically protein filaments that grow from follicles in the dermis of mammals. Their surfaces are composed of cuticle cells and other lipids. The gradual growth of HH and RF result in their rough surfaces with wave-like structures, as shown in Figure 1B and C. The average diameter of HH is 88.1 ± 8.6 μm, while it is 13.1 ± 0.8 μm for RF.

A CNF in water solution with a CNF concentration of 1 wt.% was prepared from commercially supplied bleached eucalyptus Kraft pulp using a TEMPO-oxidation method according to our previously described procedures.[46, 47] To prepare highly porous CNF-based composite aerogel films, three fillers with solid weights equal to that of CNF were dispersed into CNF solutions via mechanical string at 1000 rpm for 1 h. The resultant solutions had a total solid concentration of 2 wt.%. They were either directly used or diluted with DI water to obtain 1 wt.% solutions. In addition, a 2% CNF solution was prepared/concentrated by a rotary evaporation. All solutions were frozen in a dry-ice/acetone bath followed by freeze drying for 3 days to obtain three-dimensional (3D) aerogels. The aerogels were then compressed at 1 MPa to prepare aerogel films. Figure S2 shows TEM images of CNF and SEM images of CNF aerogels prepared from the 1% solution to form a nanofibrillar porous structure. Figure 1D–F shows the morphology of the CNF/SF aerogel. The CNF/SF aerogel surface was less porous, while nanosized pores could be observed from the inset image (Figure 1E). SFs were exposed on the surface and uniformly distributed in the aerogel (Figure 1F). Black HHs and faint-yellow RFs can be seen on the aerogel surfaces (Figure 1G and J).

CNF in the CNF/HH and CNF/RF aerogels formed similar nanofibrillar porous structures as the CNF aerogels as shown in the high magnification insets in Figure 1H and K, and HHs and RFs were well distributed in the cross section of the aerogel (Figure 1I and L). For the aerogels prepared from 2% solutions, the surface of all aerogels showed inferior porous structures compared to their counterparts prepared from the 1% solutions, as shown in Figure S3. This was because the increased solid concentration caused the formation of some CNF films instead of nanofibrils, thus more porous structures were obtained with less material for the aerogels.

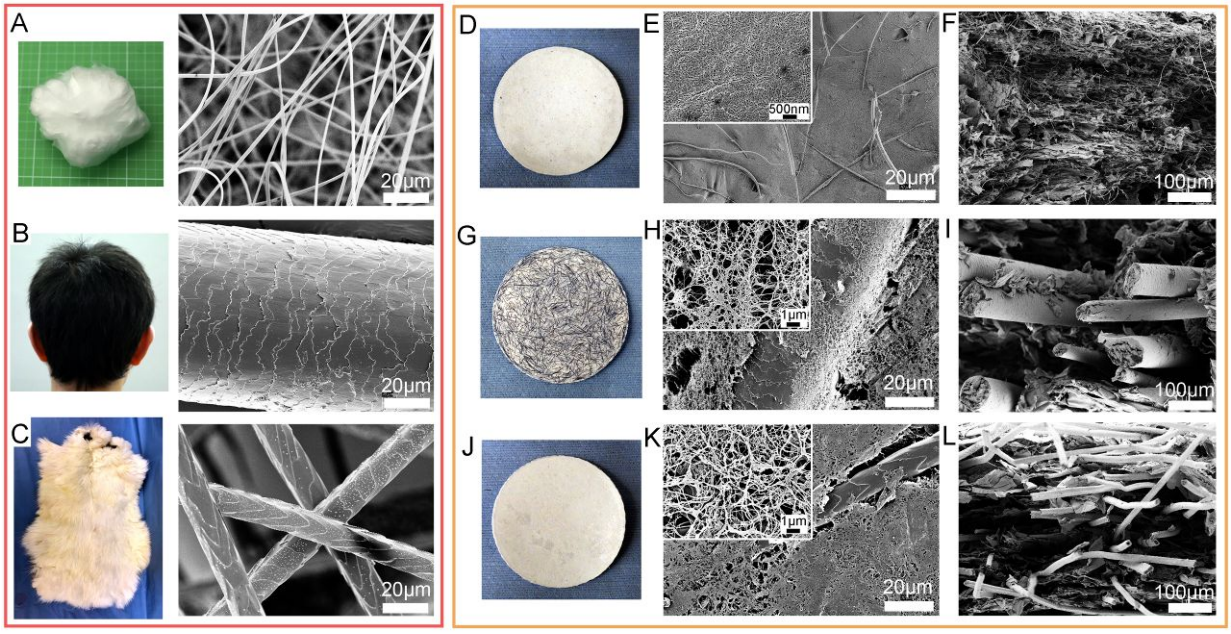

Figure 1. Morphological characterization of fillers and composite aerogels. (A–C) Digital photographs and corresponding SEM images of silica fiber, human hair, and rabbit fur, respectively. (D, G, J) Digital photographs, (E, H, K) surface morphology, and (F, I, L) cross-section morphology of (D–F) CNF/SF, (G–I) CNF/HH, and (J-L) CNF/RF composite aerogel films.

The physical, mechanical, and biological properties of the CNF-based composite aerogels were investigated systematically. It was found that the addition of fillers significantly increased the viscosity of the CNF solution, which might be attributed to the entanglements among the fillers and the hydrogen bonds formed between the fillers and the CNF since there are abundant amino and thiol groups present in the amino acids in human hair[48] (Figure 2A). The bulk density and surface area of the aerogel films prepared with 1% solutions are shown

in Figure 2B and Table 1. The CNF/SF aerogel showed the highest density of 0.21 g/cm^3 due to the high density of silica, while all of the other aerogels had a lower density of about 0.17 g/cm^3. The surface area for the CNF aerogel, however, was significantly higher than the other aerogels due to its highly porous nanofibrillar structure. The CNF/SF aerogel showed the lowest surface area because it lacks a highly porous structure (c.f. Figure 1E). The surface area of the CNF/RF aerogel was greater than that of the CNF/HH aerogel since RF had a smaller diameter and a higher surface area-to-volume ratio than HH. We also found that the bulk density and surface area of the aerogels prepared from 2% solutions showed the same trend as their counterpart aerogels prepared from 1% solutions, while their densities were higher and their surface areas were lower (Figure 2C and Table 1), which agreed with the SEM observations. The compressive properties of the as-prepared 3D aerogels and compressed aerogel films were measured as shown in Figure 2D–F. Both the compressive modulus and the tensile modulus improved dramatically with the addition of the three kinds of fillers, with RF exhibiting the maximum improvement, followed by SF and HH. It was found that RF possessed a better reinforcement effect than HH, and it also greatly increased the strain-at-yield and strain-at-break in tensile tests (Figure 2F).

Table 1. Surface areas of CNF and CNF-based composite aerogel films made of solutions with 1% or 2% concentrations. (Unit: m^2/g)

Solution concentration	CNF aerogel film	CNF/SF aerogel film	CNF/HH aerogel film	CNF/RF aerogel film
1% solution	50.7	28.9	33.2	37.8
2% solution	41.3	15.2	18.8	22.9

Moreover, we investigated the cytotoxicity and biocompatibility of these CNF composite aerogel films by culturing HEF1 human fibroblasts on them for up to 10 days. We previously

verified the biocompatibility of SF[44]. Interestingly, we also found that HH and RF greatly enhanced the cell proliferation on CNF. As shown from the live/dead assay (Figure 2G and Figure S4), dead cells (indicated by red fluorescence) can be barely seen at both day 3 and day 10, and the statistical results suggest that the cell viability was over 90% at day 3 and over 95% at day 10 for all CNF composite aerogels (Figure S5A). Cell proliferation, which was assessed via MTS assays, indicated that the number of cells on CNF/HH and CNF/RF aerogels were significantly higher than on other aerogels at both day 3 and day 10 (Figure S5B). From the cytoskeleton images (Figure 2H), cell filaments and filopodia can be clearly seen, thus indicating a healthy phenotype. Therefore, these results indicate the CNF composite aerogels prepared are nontoxic to human cells and, thus, have potential to be used in biomedical applications.

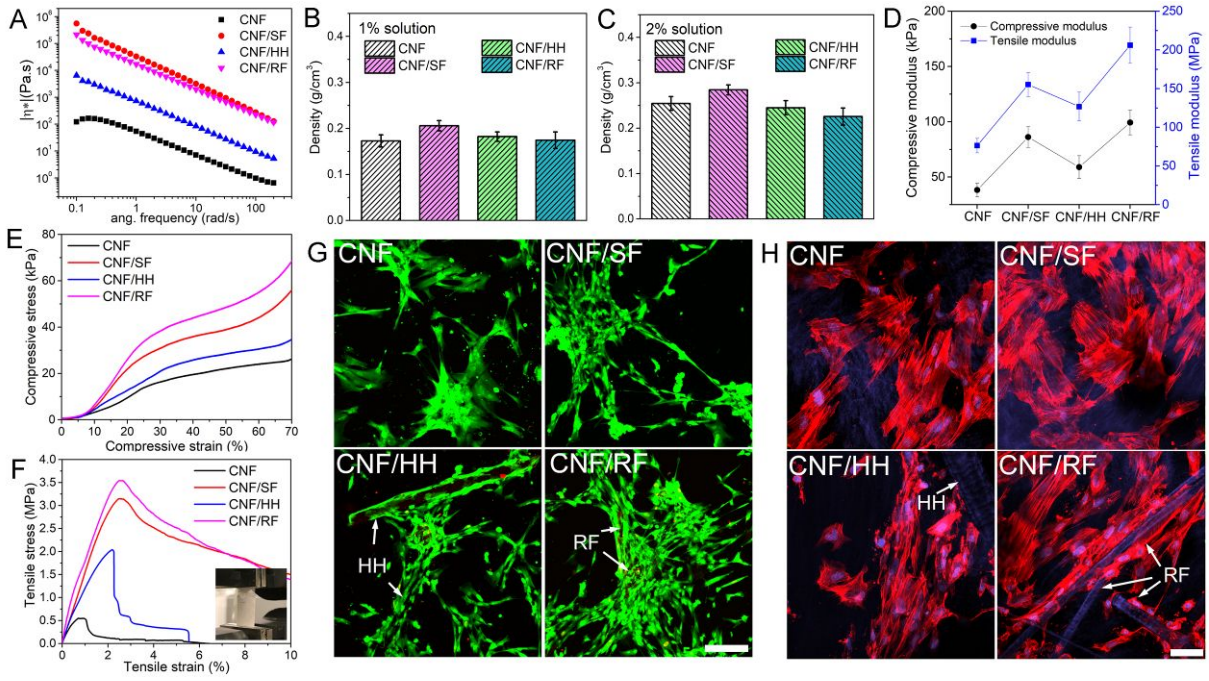

Figure 2. Properties of CNF and CNF-based composite aerogels. (A) Viscosity of CNF and CNF composite solutions. Bulk density of CNF and CNF-based composite aerogel films made of (B) 1% solutions and (C) 2% solutions. (D) Compressive moduli of as-prepared aerogels and tensile moduli of compressed aerogel films. (E) Representative compression and (F) tensile test curves of as-prepared aerogels and compressed aerogel films. Fluorescence images of HEF1 human fibroblasts cultured on CNF and CNF-based composite aerogels for 3 days: (G) live/dead images stained with green fluorescence (Calcein-AM) indicates live cells, while red fluorescence (EthD-1) indicates dead cells (scale bar = 200 μm). (H) Cytoskeleton stained images with red fluorescence (Phalloidin) indicates cell skeleton and blue fluorescence (DAPI) indicates cell nuclei (scale bar = 100 μm).

Next the triboelectric output performance of these CNF-based composite aerogels was investigated. It is known that the tribopositivity of RF, HH, and glass are in the top tier of the triboelectric series, which is attributed to their ability to lose electrons.[25, 26] X-ray photo-electron spectroscopy (XPS) was used to characterize the surface chemistry of the three fillers (Figure S6). SF is composed of silicon dioxide, which has a high tendency to lose electrons. It was interesting to find that HH and RF had similar chemical compositions on their surfaces (Figure S6B and C). The amino and thiol groups in HH and RF are bioactive groups and have strong electron-donating attributes, which contributed to their high tribopositivity.[49] We believe it is the smaller fiber diameter of SF that led to its higher tribopositivity, as compared to HH, given that they have similar chemical compositions on their surfaces. These materials are rarely used in TENG applications likely due to the brittleness of silica and the difficulties in processing HH and RF. Integrating these materials into porous CNF aerogels as fillers provides a feasible way to utilize them in TENG fabrication.

To assemble TENGs, another tribonegative material is required to create a high electro-static potential. Here, we used polyimide (PI) aerogel films reported in our previous work[35, 50] as the tribonegative material. The PI aerogel is highly flexible (Figure 3B) and porous, with a porosity of 92%. The surface of the PI aerogel exhibited a nanoporous structure (Figure 3A) and its cross section was comprised of numerous nanofibrils (Figure 3C) that contributed to an extremely high surface area of 212 m^2/g. Figure 3D depicts the schematic of the assembled PCTENG device with the CNF composite aerogel as the tribopositive material and the PI aerogel as the tribonegative material. The triboelectric materials were attached to flexible indium tin oxide (ITO)-coated polyethylene terephthalate (PET) substrates as current collectors, which were separated by two PDMS spacers. The fabricated TENG had an effective contact area of 2 cm^2 and excellent flexibility, as shown in Figure 3E. With regard to compatibility in humans, the biocompatibility of PI, PET, and ITO has been well confirmed in

the literature.[51-53] In this study, we verified the biocompatibility of CNF composite aerogels containing various fillers. Thus, the developed TENGs are fully made of biocompatible materials, thereby enabling their potential application in biomedical devices.

The working principle for the novel porous composite TENG is depicted in Figure 3F. Upon contact, opposite charges are generated on both of the triboelectric materials through the effect of contact electrification and electrostatic induction.[54, 55] When the two materials start to release, an electrostatic potential is created between the two current collectors, which drives the flow of electrons from the top current collector to the bottom current collector.[56, 57] This causes the electrostatic potential to increase to a peak value when the TENG is fully release. Similarly, electrons are pushed back from the bottom current collector to the top current collector when the TENG is pressed again since the electrostatic potential difference is compensated for by the opposite charges on both triboelectric materials. The inset image shows an example of the voltage signal in one pressing and releasing cycle. Thereby, energy can be harvested and stored by this repeating mechanical motion. Hence, the amount of charges generated on the triboelectric materials determines the output efficiency of the TENG. Specifically for our PCTENGs, the high surface area of the highly porous aerogels enables the generation and accumulation of charges not only on the surface, but also inside of the material.[35, 58] The addition of fillers with high tribopositivity enhanced the ability of composite aerogels to lose electrons upon contact with PI aerogels; thus, more charges were generated on both aerogels, which contributed to the improved performance of the PCTENGs.

From the triboelectric output results, it was found that the open circuit voltage (V_{oc}) for the CNF aerogel-based TENG was 44.0 V, and the short circuit current (I_{sc}) was 4.0 μA. The V_{oc} and I_{sc} increased to 52.8 V and 6.3 μA for CNF/SF aerogel-based PCTENG, 72.8 V and 8.4 μA for CNF/HH aerogel-based PCTENG, and 110.0 V and 11.3 μA for CNF/RF aerogel based-PCTENG. This dramatic improvement was mainly attributed to the high tribopositivity of the three kinds of fillers. Moreover, we also verified that the triboelectric outputs (both V_{oc}

and I_{sc}) of PCTENGs fabricated with CNF composite aerogels prepared from 2% solutions were significantly lower than the TENGs fabricated with CNF composite aerogels prepared from 1% solutions due to their lower surface areas (Figure S7). Therefore, by employing a highly porous structure, we achieved higher output performances with less material, which is highly desirable for reducing the production costs of TENGs. Figure S8 compares the performance of the eight TENGs in the study. The CNF/RF aerogel-based PCTENG showed the highest output voltage of 110 V, which is 2.5 times higher than that of the CNF aerogel-based TENG.

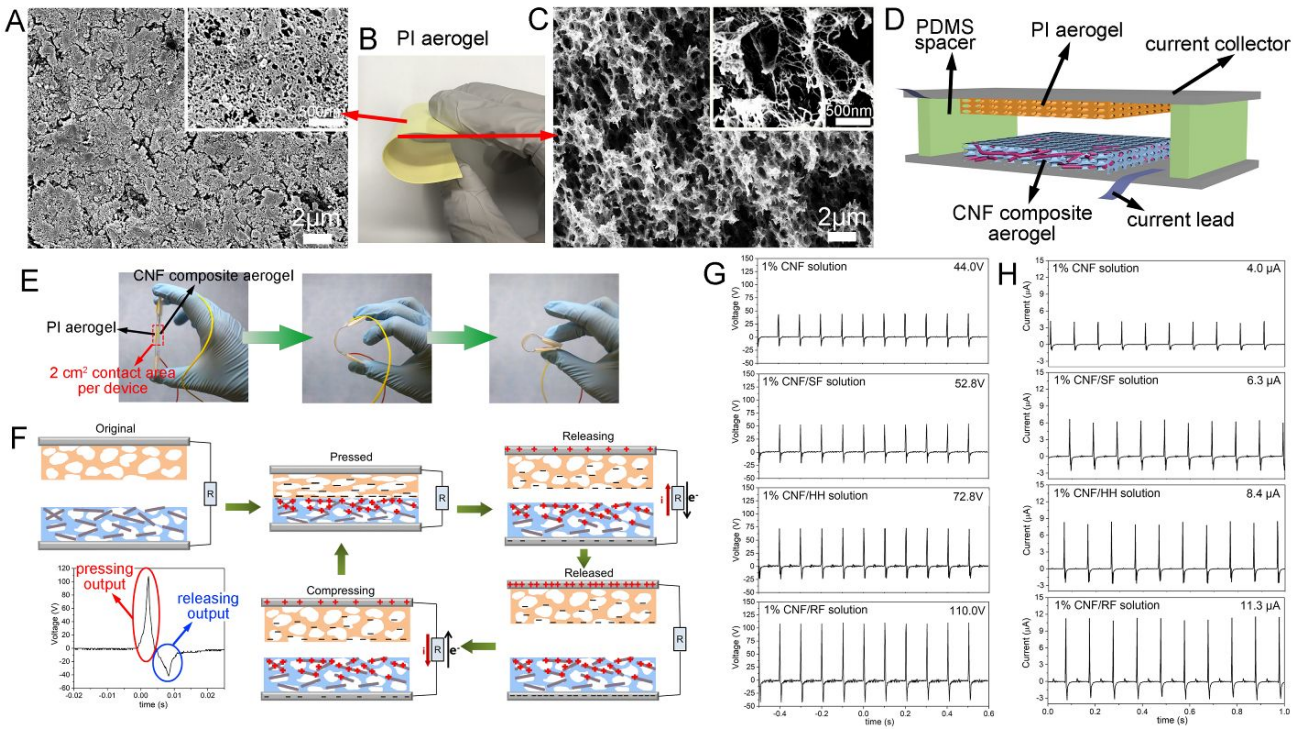

Figure 3. (A) Surface and (C) cross-section morphology of the PI aerogel. (B) A digital photograph showing the flexibility of the PI aerogel. (D) Schematic of the assembled PCTENG using the PI aerogel and the CNF composite aerogel. (E) Demonstration of a flexible TENG device with an effective contact area of 2 cm^2. (F) Diagram showing the working principle of a highly porous PI aerogel and a CNF composite aerogel-based TENG, along with the representative voltage output in one cycle of pressing and releasing. (G) Open circuit voltage and (H) short circuit current results of TENGs assembled with different CNF and CNF composite aerogels against PI aerogels.

To investigate the performance of these PCTENGs on an external load, they were connected to different resistors, with resistances ranging from 1 kΩ to 10 MΩ, and the current

density and output power density were measured (Figure 4A and Figure S9). The current density on external loads decreased with the increase in their resistance for all PCTENGs. A peak power density of 3.4 W/m^2 was achieved on a 4.7 MΩ external load for the CNF/RF aerogel-based PCTENG. However, the peak power densities were 0.5 W/m^2, 0.6 W/m^2, and 1.3 W/m^2 for CNF, CNF/SF, and CNF/HH aerogel-based TENGs, respectively. Thus, a 6.8 fold improvement in output power density was achieved by the CNF/RF aerogel-based PCTENG in comparison to the CNF aerogel-based TENG. Therefore, the CNF/RF aerogel-based PCTENG was selected in the following study to further demonstrate its energy harvesting and self-powered sensing performance. Figure 4B demonstrates the force dependence output of the CNF/RF aerogel-based PCTENG, which showed that a higher output voltage could be achieved with an increased pressing force. This implies that more electrons were transferred from CNF/RF aerogels to PI aerogels with a higher pressing force because of the tighter contact between them. The output voltage of the PCTENG showed a high dependence on the frequency of the mechanical motion as well (Figure 4C). The frequency of the output signal exactly followed the mechanical motion frequency. Meanwhile, the peak voltage was maintained as long as the compression force remained unchanged. To demonstrate the energy generation ability of the PCTENG, it was used to light 32 multi-colored LEDs connected in series through a bridge rectifier. The LEDs spelled “PCNG”, which stands for “porous composite nanogenerator”, and could be easily lit by the PCTENG (Figure 4D and Movie 1). Moreover, the PCTENG could light 60 blue LEDs, and the frequency of the emitted light showed a high dependence on the frequency of the mechanical motion (Movie 2).

TENGs generate discontinuous alternating currents, which are not suitable for directly powering most electronics. Hence, the energy harvested by the TENG is preferably stored first. To demonstrate this, our PCTENG was used to charge different capacitors at a frequency of 10 Hz and a compression force of ~6 N. As shown in Figure 4E, the PCTENG quickly

charged a 10 μF capacitor to 6 V in 173 s, a 22 μF capacitor to 6 V in 355 s, and a 100 μF capacitor to 1.5 V in 361 s. Afterwards, the harvested energy was used to light LEDs, or power electronics, such as a timer, as demonstrated in Figure 4F, Movie 3, and Movie 4. However, the stored energy was consumed rapidly since the energy consumption rate surpasses the energy generation rate of PCTENG. Thus, the capacitor needs to be charged repetitively to power the timer intermittently as shown in Figure 4G. The energy supply sustainability can be easily enhanced by increasing the size of the PCTENG and the charging time. Two PCTENGs connected in parallel, with an effective contact area of 4 cm^2, were used to charge a 1 F supercapacitor to 1.3 V in about 2 h. The harvested energy was able to continuously power a mini motor, as shown in Figure 4H and I, and Movie 5. Furthermore, device stability is an important attribute for TENGs. Figure 4J shows that the output voltage of our PCTENG was maintained while continuously running for 30 min at 10 Hz. The performance of a PCTENG stored in open air was tested over 8 weeks. As shown in Figure 4K, the PCTENG maintained a very stable output over the 8 weeks. The contact surface morphology of the CNF/RF aerogel and PI aerogel of the TENG after operating for 30 min was observed using SEM, and no obvious change in porous structure was observed (Figure S10). These results suggest that our PCTENG has high durability and stability over long-term use.

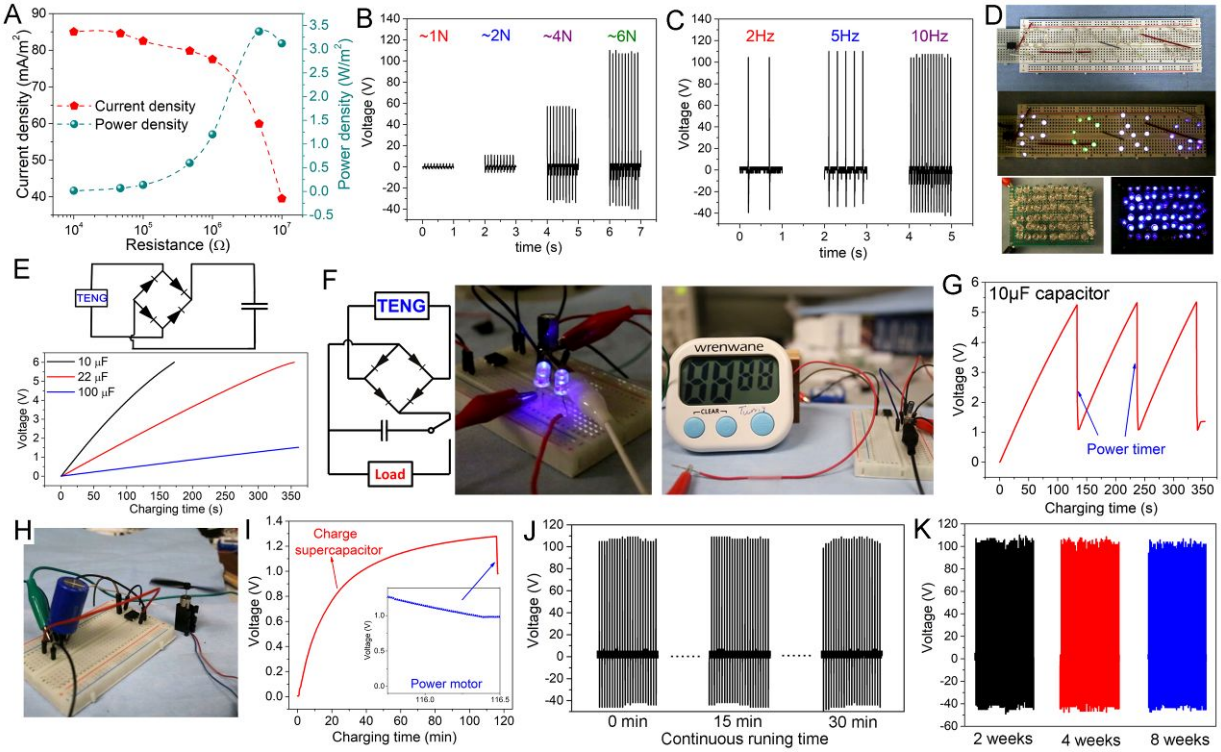

Figure 4. The energy harvesting performance of a CNF/RF aerogel and a PI aerogel-based PCTENG. (A) The current density and power density on external loads with resistances ranging from 1 kΩ to 10 MΩ. The output performance of the PCTENG under different (B) force and (C) frequency. (D) A demonstration of 34 LEDs with different colors that spell "PCNG", and 60 blue LEDs that were instantly lit by a PCTENG under 30 kPa. (E) A demonstration of the capacitor charging performance of a PCTENG through a bridge rectifier. (F) Two blue LEDs and a timer powered by the energy stored in 10 μF capacitors. (G) A 10 μF capacitor charged by the PCTENG was used to power the timer. (H) A demonstration of a motor powered by a 1 F supercapacitor charged with the PCTENG and (I) the corresponding voltage change over time. (J) The continuous output performance of the PCTENG measured during a 30 min interval at 10 Hz. (K) The output performance stability test for the PCTENG over eight weeks.

Since TENGs generate voltage signals when subjected to mechanical motion, they can be used to detect or monitor mechanical motion as well. A great advantage of TENGs in sensing applications, compared to other resistive and capacitive sensors, is their lack of a need for an external energy source.[4, 59] Therefore, TENGs are usually recognized as self-powered sensors. Moreover, if TENGs are connected to energy storage devices during sensing, they can harvest that energy simultaneously, which adds more value to TENGs.

Next, we will demonstrate the sensing performance of our CNF/RF aerogel-based PCTENG to various motions and show their ability to harvest energy from those motions.

Figure 5A and movie 6 show that our PCTENG can generate electrical signals in response to a finger tapping. The output voltage increased with increasing tapping force, and a high voltage of 72 V was achieved with a hard tap. In addition, our PCTENG was capable of detecting light forces owing to its high output performance. Figure 5B and movie 7 demonstrate that the PCTENG can detect falling water droplets on its surface. The water droplet fell from a height of ~10 cm and generated a voltage of ~0.8 V, while it was ~0.3 V when it fell from a height of ~5 cm. Moreover, it was found that the accumulated water puddle on the PCTENG surface did not affect the sensing performance, and the environmental humidity was maintained at 40% during the test, thus indicating high stability in practical applications.

Our PCTENG could also sense the vibration of the substrate it was attached to without needing direct contact with that surface (Figure 5C and movie 8). In the test, the PCTENG was placed on a wood bench, and the bench was knocked by a wood block at distances of 5 cm and 10 cm away from the PCTENG. The pace of knocking was detected by the PCTENG and the voltage was greater when the knocking location was closer to the PCTENG. Moreover, the vibration of the PCTENG caused by falling water droplets and the vibration of the wood bench was reflected by multiple descending voltage signals, as shown in Figure S11, thereby suggesting high sensing accuracy. Therefore, our PCTENG exhibited high sensitivity in detecting and monitoring light forces and small motions. Owing to the excellent flexibility of our CNF/RF aerogel-based PCTENG, it can sense bending motions as well. As demonstrated in Figure 5D and movie 9, an instant voltage of 18 V was generated with a bending angle ~30°, and the voltage output increased with an increase in bending angle.

At last, we showed the ability of our PCTENG to monitor human walking pace and harvest energy at the same time. For a simple demonstration, a PCTENG (with a 2 cm^2 effective contact area) was taped on the shoe sole and a high instant voltage of ~58 V was generated during normal human walking, as shown in Figure 5E and movie 10. The positive

and negative signals indicate the energy generated during step on and step off, respectively, and the spontaneous voltage signal exactly followed the human walking pace, suggesting that our PCTENG not only acted as a pedometer, but was also capable of detecting the walking pace and walking force, as well as harvesting mechanical energy from walking.

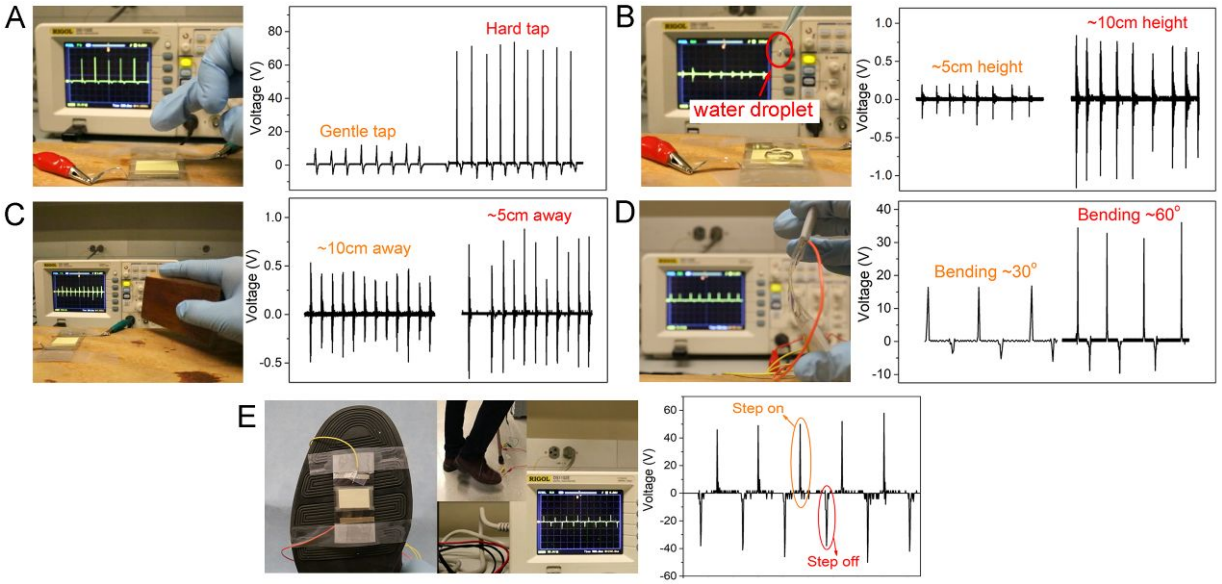

Figure 5. Self-powered sensing performance of CNF/RF aerogels and PI aerogel-based PCTENGs and their ability to harvest energy from various motions during sensing. (A) Sensing different forces applied by figure tapping. (B) Sensing falling water droplets from different heights. (C) Sensing vibrations of the substrate that the PCTENG was attached to. (D) Sensing different bending angles. (E) Sensing human walking pace using a PCTENG attached to the sole of a shoe.

Conclusions

In this study, we developed new approaches to boost the output performance of TENGs by creating highly porous structures and introducing fillers with high tribopolarities to the triboelectric materials of TENG. SF, HH, and RF were used for the first time in TENG made of highly porous materials, which resulted in better mechanical properties and, more importantly, significant triboelectric output improvements due to their high tribopositivities. We also demonstrated that CNF composite aerogel-based TENGs that were fabricated from low concentration solutions exhibited higher surface areas and superior output performances, thus suggesting a feasible way to simultaneously reduce the material cost and increase the performance of the TENGs. The CNF/RF aerogel-based PCTENGs showed the highest

energy generation ability. They possessed a high output power density of 3.4 W/m^2 on a 4.7 MΩ external load under a pressure of 30 kPa, which is 6.8 times that of the CNF aerogel-based TENG. The PCTENG showed excellent performance in lighting LEDs, charging capacitors, and powering small electronics. Owing to their high output performance and flexibility, the PCTENG exhibited a versatile, self-powered sensing ability towards light forces, like falling water droplets and substrate vibration, bending, figure tapping, and human walking. This work provides new directions and guidelines for the design and fabrication of low cost, high performance, biocompatible and flexible TENGs that are widely applicable in ambient mechanical energy harvesting, wearable electronics, and flexible self-powered sensors.

Experimental Section

Fabrication of CNF Composite Aerogels:

CNF with a concentration of 1 wt.% in water was prepared from commercially supplied bleached eucalyptus Kraft pulp (Aracruz Cellulose, Brazil) according to our previously described procedures. [46] SF, HH, and RF fillers were mixed in a CNF solution at a 1:1 weight ratio to CNF, yielding a 2% solid-content solution. To prepare 1% solid-content solution, an equal volume of water was added to the above solution. The solution was mixed via mechanical stirring at 100 rpm for 30 min. The freshly prepared solution was poured into aluminum dishes, followed by freezing in a dry-ice/acetone bath (–78 °C) and freeze drying using a freeze dryer (Labconco) at –83 °C and 0.04 mBar for 3 days to obtain aerogels. The aerogels were then compressed at a pressure of 1.0 MPa using a universal mechanical property test instrument (Instron) to obtain the aerogel films.

General Characterizations:

The microstructures were imaged using a fully digital LEO GEMINI 1530 (Zeiss) at an acceleration voltage of 3 kV. All samples were sputtered with a thin film of gold before imaging. XPS measurements were performed on an XPS instrument with a focused, monochromatic K-alpha X-ray source and a monoatomic/cluster ion gun (Thermo Scientific). The bulk densities were calculated by measuring the mass and volume of the specimens. All specimens were pre-dried in vacuum oven for 5 h at 50 °C. The Brunauer–Emmett–Teller (BET) surface area was measured using a Gemini VII 2390 surface area analyzer (Micromeritics Instrument Corp.). The viscosities of the CNF composite solutions were tested using a rheometer (AR 2000ex, TA) equipped with a 25 mm 2º cone–plate geometry at 25 ºC. Oscillatory frequency sweep tests were performed at a constant stress of 1 Pa, with an increasing angular frequency from 1 to 200 rad/s. The compression and tensile tests of fabricated aerogels were carried out on a universal mechanical property test instrument (Instron) with a crosshead speed of 1 mm/min for both tests. At least three specimens were measured to obtain the average value and standard deviation.

PCTENG Device Fabrication and Performance Characterization:

To fabricate the PCTENG device, CNF composite and PI aerogel films were cut into 1 cm × 2 cm rectangles and attached to two ITO-coated flexible PET substrates (surface resistivity of 60 Ω/sq). The two pieces were assembled face-to-face and separated by two PDMS spacers (3 mm thick) to create an air gap between them. The generated electrical signals were led out through two aluminum strips fixed on both ITO/PET substrates. A shaker (LDS V201, Brüel & Kjær, Denmark) was used to provide the input of the mechanical motion. A function generator (B&K Precision) and a sound stereo receiver (Yamaha) were used to control the frequency and force, respectively. The voltage signal generated was recorded using an oscilloscope (DS1102E, Rigol) and the current signal was recorded using a potentiostat (versaSTAT-3, Princeton Applied Research). The output power density was calculated using

$PD_o = I^2R / A$, where I was the peak current, R was the resistance of the external load, and A was the effective area of the TENG.

Acknowledgements

The authors would like to acknowledge the financial support of the National Natural Science Foundation of China (51603075; 21604026), USDA Forest Service, P3Nano (E17-21), and the Wisconsin Institute for Discovery (WID) at the University of Wisconsin–Madison. Great appreciation is given to Mary Ann B. Meador of the NASA Glenn Research Center, and Haiquan Guo of the Ohio Aerospace Institute for producing the PI aerogel film used in this study.

Supplementary Information:

Electronic Supplementary Information (ESI) available: detailed experimental procedures, TEM and SEM images, fluorescence images of HEF1 cells at day 10, cell viability and proliferation assays, XPS, additional triboelectric output performance and power density results, and sensing performance. See DOI: 10.1039/x0xx00000x

Notes and References

1. Y. F. Tang, Q. F. Zheng, B. Chen, Z. Q. Ma and S. Q. Gong, *Nano Energy*, 2017, **38**, 401-411.
2. J. Deng, X. Kuang, R. Liu, W. Ding, A. C. Wang, Y. C. Lai, K. Dong, Z. Wen, Y. Wang, L. Wang, H. J. Qi, T. Zhang and Z. L. Wang, *Adv. Mater.*, 2018, **30**, 1705918.
3. X. X. Chen, M. D. Han, H. T. Chen, X. L. Cheng, Y. Song, Z. M. Su, Y. G. Jiang and H. X. Zhang, *Nanoscale*, 2017, **9**, 1263-1270.
4. !!! INVALID CITATION !!!
5. C. Xu, Y. L. Zi, A. C. Wang, H. Y. Zou, Y. J. Dai, X. He, P. H. Wang, Y. C. Wang, P. Z. Feng, D. W. Li and Z. L. Wang, *Adv. Mater.*, 2018, **30**.

6. C. Xu, A. C. Wang, H. Y. Zou, B. B. Zhang, C. L. Zhang, Y. L. Zi, L. Pan, P. H. Wang, P. Z. Feng, Z. Q. Lin and Z. L. Wang, *Adv. Mater.*, 2018, **30**.
7. Z. L. Wang, *Faraday Discuss*, 2014, **176**, 447-458.
8. Y. J. Su, Y. Yang, X. D. Zhong, H. L. Zhang, Z. M. Wu, Y. D. Jiang and Z. L. Wang, *ACS Appl. Mater. Interfaces*, 2014, **6**, 553-559.
9. B. B. Zhang, J. Chen, L. Jin, W. L. Deng, L. Zhang, H. T. Zhang, M. H. Zhu, W. Q. Yang and Z. L. Wang, *Acs Nano*, 2016, **10**, 6241-6247.
10. S. Lee, Y. Lee, D. Kim, Y. Yang, L. Lin, Z. H. Lin, W. Hwang and Z. L. Wang, *Nano Energy*, 2013, **2**, 1113-1120.
11. Z. L. Wang, T. Jiang and L. Xu, *Nano Energy*, 2017, **39**, 9-23.
12. X. D. Zhong, Y. Yang, X. Wang and Z. L. Wang, *Nano Energy*, 2015, **13**, 771-780.
13. T. Huang, C. Wang, H. Yu, H. Z. Wang, Q. H. Zhang and M. F. Zhu, *Nano Energy*, 2015, **14**, 226-235.
14. S. W. Chen, C. Z. Gao, W. Tang, H. R. Zhu, Y. Han, Q. W. Jiang, T. Li, X. Cao and Z. L. Wang, *Nano Energy*, 2015, **14**, 217-225.
15. S. L. Zhang, M. Y. Xu, C. L. Zhang, Y. C. Wang, H. Y. Zou, X. He, Z. J. Wang and Z. L. Wang, *Nano Energy*, 2018, **48**, 421-429.
16. X. Pu, L. X. Li, H. Q. Song, C. H. Du, Z. F. Zhao, C. Y. Jiang, G. Z. Cao, W. G. Hu and Z. L. Wang, *Adv. Mater.*, 2015, **27**, 2472-2478.
17. Q. Zheng, Y. Zou, Y. L. Zhang, Z. Liu, B. J. Shi, X. X. Wang, Y. M. Jin, H. Ouyang, Z. Li and Z. L. Wang, *Science Advances*, 2016, **2**.
18. W. Li, D. Torres, R. Diaz, Z. J. Wang, C. S. Wu, C. Wang, Z. L. Wang and N. Sepulveda, *Nat Commun*, 2017, **8**.
19. D. Klemm, B. Heublein, H.-P. Fink and A. Bohn, *Angewandte Chemie International Edition*, 2005, **44**, 3358-3393.
20. D. Klemm, F. Kramer, S. Moritz, T. Lindstrom, M. Ankerfors, D. Gray and A. Dorris, *Angew Chem Int Edit*, 2011, **50**, 5438-5466.
21. R. J. Moon, A. Martini, J. Nairn, J. Simonsen and J. Youngblood, *Chem Soc Rev*, 2011, **40**, 3941-3994.
22. C. Yao, X. Yin, Y. Yu, Z. Cai and X. Wang, *Adv. Funct. Mater.*, 2017, **27**, 1700794.
23. H. Y. Mi, X. Jing, Q. Zheng, L. Fang, H. X. Huang, L. S. Turng and S. Gong, *Nano Energy*, 2018, **48**, 327-336.
24. Y. C. Mao, N. Zhang, Y. J. Tang, M. Wang, M. J. Chao and E. J. Liang, *Nanoscale*, 2017, **9**, 14499-14505.

25. K. L. Kaiser, *Electrostatic Discharge*, CRC Press, Boca Raton, 2006.
26. D. K. Davies, *J Phys D Appl Phys*, 1969, **2**, 1533-1537.
27. J. S. Chun, B. U. Ye, J. W. Lee, D. Choi, C. Y. Kang, S. W. Kim, Z. L. Wang and J. M. Baik, *Nat Commun*, 2016, **7**, 12985.
28. L. M. Zhang, C. B. Han, T. Jiang, T. Zhou, X. H. Li, C. Zhang and Z. L. Wang, *Nano Energy*, 2016, **22**, 87-94.
29. L. Lin, S. H. Wang, Y. N. Xie, Q. S. Jing, S. M. Niu, Y. F. Hu and Z. L. Wang, *Nano Lett.*, 2013, **13**, 2916-2923.
30. Q. Li, A. Peer, I. H. Cho, R. Biswas and J. Kim, *Nat Commun*, 2018, **9**.
31. V. Nguyen and R. S. Yang, *Nano Energy*, 2013, **2**, 604-608.
32. Y. Yang, H. L. Zhang, Y. Liu, Z. H. Lin, S. Lee, Z. Y. Lin, C. P. Wong and Z. L. Wang, *Acs Nano*, 2013, **7**, 2808-2813.
33. W. Q. Yang, J. Chen, Q. S. Jing, J. Yang, X. N. Wen, Y. J. Su, G. Zhu, P. Bai and Z. L. Wang, *Adv. Funct. Mater.*, 2014, **24**, 4090-4096.
34. R. X. Wang, S. J. Gao, Z. Yang, Y. L. Li, W. N. Chen, B. X. Wu and W. Wu, *Adv. Mater.*, 2018, **30**.
35. Q. Zheng, L. Fang, H. Guo, K. Yang, Z. Cai, M. A. B. Meador and S. Gong, *Adv. Funct. Mater.*, 2018, **28**, 1706365.
36. Z. Li and Y. W. Yang, *J. Mater. Chem. B*, 2017, **5**, 9278-9290.
37. H. Liu, X. X. Liu, W. Li, X. Guo, Y. Wang, G. X. Wang and D. Y. Zhao, *Adv. Energy Mater.*, 2017, **7**, 1700283.
38. Q. F. Cheng, C. J. Huang and A. P. Tomsia, *Adv. Mater.*, 2017, **29**, 1703155.
39. Y. Yang and Z. L. Wang, *Nano Energy*, 2015, **14**, 245-256.
40. Y. C. Wu, X. D. Zhong, X. Wang, Y. Yang and Z. L. Wang, *Nano Res.*, 2014, **7**, 1631-1639.
41. S. H. Wang, X. J. Mu, Y. Yang, C. L. Sun, A. Y. Gu and Z. L. Wang, *Adv. Mater.*, 2015, **27**, 240-248.
42. H. Y. Mi, X. Jing, H. Xie, H. X. Huang and L. S. Turng, *Chem. Eng. J.*, 2018, **337**, 541-551.
43. H. Y. Mi, X. Jing, H. X. Huang and L. S. Turng, *Mater. Lett.*, 2017, **204**, 45-48.
44. H. Y. Mi, X. Jing, B. N. Napiwocki, Z. T. Li, L. S. Turng and H. X. Huang, *Chem. Eng. J.*, 2017, **331**, 652-662.
45. H. Y. Mi, X. Jing, H. X. Huang and L. S. Turng, *Mater. Lett.*, 2017, **210**, 173-176.

46. H. Y. Mi, X. Jing, M. R. Salick, T. M. Cordie and L. S. Turng, *J Mech Behav Biomed*, 2016, **62**, 417-427.
47. H. Y. Mi, X. Jing, A. L. Politowicz, E. Chen, H. X. Huang and L. S. Turng, *Carbon*, 2018, **132**, 199-209.
48. C. R. Robbins, in *Chemical and Physical Behavior of Human Hair*, ed. C. R. Robbins, Springer, Berlin2012, ch. 2, pp. 105-176.
49. E. N. Jayaweera, K. R. Wijewardhana, T. K. Ekanayaka, A. Shahzad and J. K. Song, *ACS Sustainable Chem. Eng.*, 2018, **6**, 6321-6327.
50. H. Guo, M. A. B. Meador, L. McCorkle, D. J. Quade, J. Guo, B. Hamilton and M. Cakmak, *Acs Appl Mater Inter*, 2012, **4**, 5422-5429.
51. R. R. Richardson, J. A. Miller and W. M. Reichert, *Biomaterials*, 1993, **14**, 627-635.
52. H. Seitz, S. Marlovits, I. Schwendenwein, E. Muller and V. Vecsei, *Biomaterials*, 1998, **19**, 189-196.
53. J. W. Wang, L. P. Wang, J. W. Di and Y. F. Tu, *Sensor Actuat B-Chem*, 2008, **135**, 283-288.
54. F. R. Fan, W. Tang and Z. L. Wang, *Adv. Mater.*, 2016, **28**, 4283-4305.
55. Z. L. Wang, *Acs Nano*, 2013, **7**, 9533-9557.
56. X. Wang, S. H. Wang, Y. Yang and Z. L. Wang, *Acs Nano*, 2015, **9**, 4553-4562.
57. H. L. Zhang, Y. Yang, X. D. Zhong, Y. J. Su, Y. S. Zhou, C. G. Hu and Z. L. Wang, *Acs Nano*, 2014, **8**, 680-689.
58. H. Y. Mi, X. Jing, M. A. B. Meador, H. Q. Guo, L. S. Turng and S. Q. Gong, *ACS Appl. Mater. Interfaces*, 2018, **10**, 30596-30606.
59. S. L. Zhang, Y. C. Lai, X. He, R. Y. Liu, Y. L. Zi and Z. L. Wang, *Adv. Funct. Mater.*, 2017, **27**.

Table of Contents

A cellulose-based highly porous composite triboelectric nanogenerator (PCTENG) with excellent energy generation performance and self-powered sensing sensitivity has been developed by introducing rabbit fur into a cellulose aerogel though an environmental friendly freeze-drying method. The improvements can be attributed to the high tribopositivity of rabbit fur and the high surface area of aerogel. This work provides new approaches for high performance TENG designing and fabrication.